

Electrodeposition of InSb branched nanowires: Controlled growth with structurally tailored properties

Suprem R. Das, Cem Akatay, Asaduzzaman Mohammad, Mohammad Ryan Khan, Kosuke Maeda, Russell S. Deacon, Koji Ishibashi, Yong P. Chen, Timothy D. Sands, Muhammad A. Alam, and David B. Janes

Citation: *Journal of Applied Physics* **116**, 083506 (2014); doi: 10.1063/1.4893704

View online: <http://dx.doi.org/10.1063/1.4893704>

View Table of Contents: <http://scitation.aip.org/content/aip/journal/jap/116/8?ver=pdfcov>

Published by the [AIP Publishing](#)

Articles you may be interested in

[In-situ energy dispersive x-ray diffraction study of the growth of CuO nanowires by annealing method](#)
J. Appl. Phys. **114**, 144303 (2013); 10.1063/1.4824177

[Improved photoelectrochemical performance of Cu\(In,Ga\)Se₂ thin films prepared by pulsed electrodeposition](#)
J. Renewable Sustainable Energy **5**, 031602 (2013); 10.1063/1.4807615

[Study on the structural and physical properties of ZnO nanowire arrays grown via electrochemical and hydrothermal depositions](#)
J. Appl. Phys. **110**, 094310 (2011); 10.1063/1.3657843

[Growth of size and density controlled GaAs / In_xGa_{1-x}As / GaAs \(x = 0.10 \) nanowires on anodic alumina membrane-assisted etching of nanopatterned GaAs](#)
J. Vac. Sci. Technol. B **28**, 1111 (2010); 10.1116/1.3498753

[In situ growth of aligned CdS nanowire arrays on Cd foil and their optical and electron field emission properties](#)
J. Appl. Phys. **104**, 014312 (2008); 10.1063/1.2952013



AIP | Journal of Applied Physics

Journal of Applied Physics is pleased to announce **André Anders** as its new Editor-in-Chief

Electrodeposition of InSb branched nanowires: Controlled growth with structurally tailored properties

Suprem R. Das,^{1,2} Cem Akatay,^{3,2} Asaduzzaman Mohammad,^{1,2} Mohammad Ryyan Khan,¹ Kosuke Maeda,^{4,5} Russell S. Deacon,^{5,6} Koji Ishibashi,^{5,6} Yong P. Chen,^{1,2,7} Timothy D. Sands,^{1,3,2} Muhammad A. Alam,¹ and David B. Janes^{1,2,a)}

¹School of Electrical and Computer Engineering, Purdue University, West Lafayette, Indiana 47907, USA

²Birck Nanotechnology Center, Purdue University, West Lafayette, Indiana 47907, USA

³School of Materials Engineering, Purdue University, West Lafayette, Indiana 47907, USA

⁴Department of Materials Science and Engineering, Tokyo Institute of Technology, 4259 Nagatsuta-cho, Midori-ku, Yokohama 226-8502, Japan

⁵Advanced Device Laboratory, RIKEN, 2-1 Hirosawa, Wako, Saitama 351-0198, Japan

⁶RIKEN Center for Emergent Matter Science (CEMS), 2-1 Hirosawa, Wako, Saitama 351-0198, Japan

⁷Department of Physics and Astronomy, Purdue University, West Lafayette, Indiana 47907, USA

(Received 10 May 2014; accepted 21 July 2014; published online 25 August 2014)

In this article, electrodeposition method is used to demonstrate growth of InSb nanowire (NW) arrays with hierarchical branched structures and complex morphology at room temperature using an all-solution, catalyst-free technique. A gold coated, porous anodic alumina membrane provided the template for the branched NWs. The NWs have a hierarchical branched structure, with three nominal regions: a “trunk” (average diameter of 150 nm), large branches (average diameter of 100 nm), and small branches (average diameter of sub-10 nm to sub-20 nm). The structural properties of the branched NWs were studied using scanning transmission electron microscopy, transmission electron microscopy, scanning electron microscopy, x-ray diffraction, energy dispersive x-ray spectroscopy, and Raman spectroscopy. In the *as-grown* state, the small branches of InSb NWs were crystalline, but the trunk regions were mostly nanocrystalline with an amorphous boundary. Post-annealing of NWs at 420 °C in argon produced single crystalline structures along $\langle 311 \rangle$ directions for the branches and along $\langle 111 \rangle$ for the trunks. Based on the high crystallinity and tailored structure in this branched NW array, the effective refractive index allows us to achieve excellent antireflection properties signifying its technological usefulness for photon management and energy harvesting. © 2014 AIP Publishing LLC.

[<http://dx.doi.org/10.1063/1.4893704>]

I. INTRODUCTION

Semiconducting nanowires (NWs) with complex morphologies (structure, length, diameter, roughness, etc.) are of considerable interest for new generation of nanoelectronics, nanophotonics, optoelectronics/photovoltaic, thermoelectric and bio-electronic devices because of their uniquely tunable physical properties that are not realizable in their bulk counterparts.^{1–5} Several different approaches to NW growth have been proposed.^{6–8} Nanowire growth using chemical vapor deposition (CVD) typically employs the vapor-liquid-solid (VLS) mechanism, with NW diameter controlled by catalyst particle size and growth conditions.⁶ While VLS growth can achieve tapered NWs and branching via regrowth from sidewalls, it is difficult to achieve hierarchical branched structures comparable to those described in the current work. Electrodeposition methods using a pre-designed growth template can provide a route to realize nanowire arrays with tailored morphologies and complex structures.^{9,10} Other advantages such as achieving sharp hetero-interfaces (for an axial and/or co-axial NW geometry), catalyst free nanowire

growth, and dealing with elements with low and high vapor pressures (e.g., in NWs with two or more elements such as In and Sb in InSb NW) make the solution-phase electrodeposition growth an attractive approach.^{11–16} For some material systems, electrodeposition can be performed at or near room temperature (RT).^{17–19} Reasonable room temperature device performance has been demonstrated in transistors employing electrodeposited nanowires.²⁰

Recently, there has been a growing interest in exploring fundamental issues and technological implications of the light-matter interactions in semiconducting nanowire arrays. Specifically, for example, size-quantization and dielectric confinement related to the size (e.g., diameter/length), shape (e.g., taper), and periodicity of the NWs have been engineered for applications in NW-based photovoltaics and photodetectors with considerable success.^{21–27} The versatility of the structure arises from the fact that two fundamental length scales, namely, the extinction distance and the minority carrier diffusion length, can be effectively decoupled in a device with NW arrays. Tapered or stepped structures, including nano-needle nanowires (NNNW) and dual-diameter nanowires (DDNW) have shown enhanced light trapping and absorption, in comparison to nanowires with a uniform diameter along their length. Therefore, growing NW

^{a)}Author to whom correspondence should be addressed. Electronic mail: janes@ecn.purdue.edu

arrays with complex architecture with phase pure material is crucial for developing devices for novel applications.

From a material prospective, InSb is a promising candidate for high speed and low power nanoelectronic devices due to its low electron effective mass and high carrier mobility at room temperature. Nanowires of this material are of interest for nanoelectronic, nanophotonic, and thermoelectric device applications.^{1,28,29} Due to the large spin-orbit coupling, InSb has been proposed for certain fundamental studies, including a prediction that Majorana fermions could be observed at the junction of InSb nanowire with a superconductor.^{30–32} The use of nanowires, rather than bulk materials, can mitigate lattice mismatch problems found in InSb epilayer growth.³³ Single NWs have demonstrated terahertz detection.^{28,34}

In this work, (i) we used an all-solution, catalyst free electrodeposition method to grow InSb branched nanowire (BNW) arrays at room temperature, (ii) demonstrate highly crystalline InSb NWs starting from sub-10 nm diameters to ~ 150 nm diameter following a post-annealing recipe in argon, (iii) have large-scale bottom up approach of nanowire growth that can be tuned to grow NWs starting from few hundreds of nanometers to tens of microns in length, simply by adjusting the growth potential and growth time, and (iv) finally, the BNW arrays were shown to exhibit excellent antireflection properties, one of the key requirements for vertical NW based solar cells and other photo-detector devices.

II. EXPERIMENTAL

A. Cyclic voltammetry and electrodeposition of InSb NWs

Commercially available porous anodic alumina (PAA) templates of thickness $60 \mu\text{m}$ (Anodisc 13 from Whatman) were used as templates for nanowire growth. Over most of the PAA thickness, the average pore opening was ~ 150 nm with a periodicity of ~ 440 nm. However, within $\sim 1.5 \mu\text{m}$ of one surface of the PAA, the template contains a branched network of nanopores with average diameter of ~ 100 nm and a surface region with average diameter of ~ 20 nm. This layered structure represents the template for hierarchical BNW growth. In prior studies, we have characterized the average pore diameters and distribution of diameters within each region.³⁶ The working electrode for the cyclic voltammetry experiment and the electrochemical deposition process was formed by evaporating a 100 nm Au layer on the surface of the PAA template containing the random branched structure. A three-electrode electrochemical cell with a Pt-mesh counter electrode, and an Ag/AgCl (saturated 3 M NaCl) reference electrode (0.175 V vs. Normal Hydrogen Electrode (NHE)) was employed. All potentials were reported with reference to this electrode. The electrolyte consisted of an aqueous solution containing 0.15 M InCl₃ (indium chloride), 0.1 M SbCl₃ (antimony chloride) along with complexing agents 0.36 M citric acid and 0.17 M potassium citrate, at pH 1.8.¹⁷ The presence of potassium citrate in the electrolyte shifts the reduction potential of both In³⁺ and Sb³⁺ ions to a common deposition potential that facilitates InSb

co-deposition. An EG&G PAR potentiostat/galvanostat (model 273) was used for the electrochemical studies of the ionic species.⁵⁶ NWs were studied in two states: (i) as-deposited and (ii) following an *in situ*, 2-step anneals (125 °C for 6 h and 420 °C for 4 h) in argon with a flow rate of 30 sccm.¹⁷

B. Structural and optical characterization of InSb NWs

The electron microscope images of the nanowires were captured using a Hitachi Field Emission Scanning Electron Microscope (FESEM) and FEI Titan 80–300 kV transmission electron microscopy (TEM). The Energy Dispersive X-ray (EDX) analysis was performed inside the TEM chamber. For TEM sample preparation, the PAA template was dissolved in 1 M KOH solution overnight and then the nanowires attached to the gold layer were released into isopropyl alcohol (IPA) via sonication. Few drops of solution containing NWs were released onto the TEM grid and dried. For x-ray diffraction measurements and Raman spectroscopy, the PAA template containing the nanowires was first etched back from the front surface for 8–10 min using 1 M KOH, rinsed thoroughly in DI, and then dried overnight in dry N₂. X-ray diffraction spectra of the nanowires were collected using a Bruker D800 focus powder diffractometer with Cu K α_1 wavelength of radiation ($\lambda = 1.5406 \text{ \AA}$). The Raman spectrum of InSb NWs was taken using a Jobin Yvon Explora spectrometer (Horiba) in backscattered geometry using 532 nm semiconductor laser excitation source at different power densities and 1800 rulings/inch grating settings. The reflectance spectra were measured using Perkin Elmer UV/VIS/NIR spectrophotometer (model Lambda950).

III. RESULTS AND DISCUSSION

A. BNW growth

The schematic diagram of the electrochemical cell and potentiostat circuit arrangements for the cyclic voltammetry and electrodeposition of NW arrays is shown in supplementary material Figure A1(a).⁵⁶ Prior to electrodeposition of NWs, one typically determines the equilibrium deposition potential using cyclic voltammetry and in our case, a deposition potential of between -1.0 V and -1.5 V was used (Fig. A1(b) shaded region in supplementary material⁵⁶). A detailed analysis of the cyclic voltammetry results is summarized in supplementary material (Sec. A1, and Figs. A1(b) and A1(c)).⁵⁶ Fig. 1 shows the direct electrodeposition of InSb BNWs deposited at a reduction potential of -1.5 V (vs. Ag/AgCl (sat. NaCl) reference electrode). The electrodeposition time and hence the average length of the BNWs was controlled by monitoring the deposition current (I) vs. deposition time (t) for a particular deposition voltage (for each deposition potential, the growth rate is different). The mechanism of growth evolves through four stages during the deposition process, see Fig. 1. At the beginning, a large current corresponds to the charge associated with electrical double layer. In region I, the ions must diffuse (through the creation of a diffusion layer) to the bottom of the narrow pore for the initiation of the growth process following Fick's

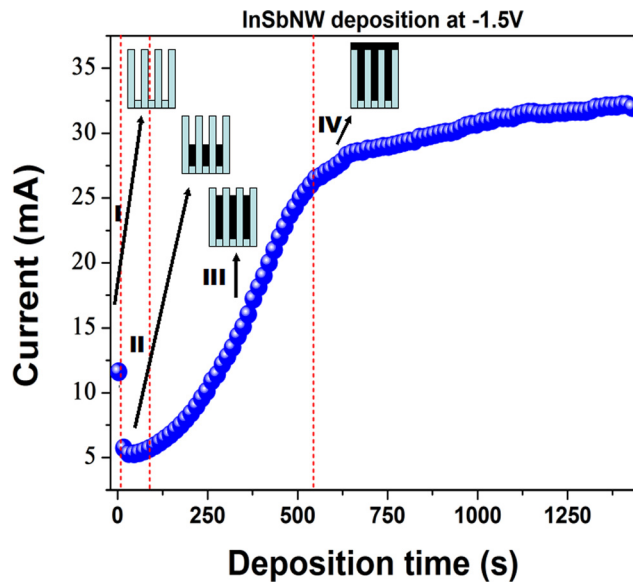


FIG. 1. Current transient of room temperature InSb nanowire growth showing different growth regimes. The current transient in different segments of the deposition process is shown schematically and discussed in the text.

first law (decrease in current). Region II is characterized by the deposition of the ions into the pore bottom but since the number of ions is still relatively small, the overall current remains almost flat and small. Region III signifies the regime with linear increase in current with the deposition time where the pores get filled rapidly until they get filled completely. At this point, the onset of the saturation of current vs. time curve was seen with visible “hemispherical shape” like capping on the nanowires heads. At the beginning of the region IV, the caps grew gradually and finally coalesced to form the film where complete saturation of the deposition current was observed. Each of these regions is associated with a constant growth rate. For additional discussions on electrode reaction mechanism and rate of NW growth, see supplementary material Sec. A2.⁵⁶ The current density is quantitatively followed by the modeling of diffusion controlled electrodeposition of metallic nanowires in high density PAA channels.³⁵

B. Characterization of the BNW

Fig. 2 shows the cross-sectional as well as the top view FESEM image of a PAA template filled with InSb nanowires for a relatively lower electrode potential (-1.0 V) for which the growth is slower. Figs. 2(a) and 2(b) show the cross-sectional view of two different PAA templates in which InSb NWs were grown for 20 min and 45 min, respectively. These durations correspond to nanowires grown in region III and the average NW lengths were $\sim 7\ \mu\text{m}$ and $\sim 15\ \mu\text{m}$, respectively, with a fill factor (defined as the fraction of pores filled by InSb) of $\sim 80\%$ in both cases. Fig. 2(c) shows the top view FESEM of one of the samples after etching back of the PAA with 1M KOH solution. The density of NWs as observed in the image is consistent with that of the cross-sectional image. Fig. 2(d) shows the average NW length vs. time in region III extracted from Fig. 2(a), Fig. 2(b), and another intermediate growth of 10 min duration. The corresponding growth rate in region III is estimated $\sim 0.34\ \mu\text{m}/\text{min}$.

Following similar analysis of deposition voltage, deposition time, and average NW length (from FESEM images) a growth rate of $\sim 1.7\ \mu\text{m}/\text{min}$ was estimated in region II and is shown in Figure A2 in supplementary material Sec. A4.⁵⁶ Note that, in each of the regions, the growth rate can be even more for a NW array grown at a higher potential such as one shown in Fig. 1. Fig. 2(e) shows the FESEM of the BNWs where the top region (note that this image is upside down of Figs. 2(a) and 2(b)) average diameter of the InSb NWs is below 20 nm, these branches merge together to form intermediate branches of average diameter $\sim 100\ \text{nm}$ ($(d,\sigma) \sim (100, 25)$) and eventually they further coalesce to form the trunk structure of InSb NW array with average diameter of $\sim 150\ \text{nm}$ ($(d,\sigma) \sim (150, 25)$). These BNWs structures could be grown on large scale templates (in our case, typically over an area with 10 mm diameter) and could be also used for other materials with applications in photon managements, energy harvesting, etc. As an immediate illustration, we will discuss below the optical reflectance of these BNWs arrays and compare with a bulk InSb wafer.

C. Crystal structure of the nanowires

Following the *in situ* anneal, the crystal structure was characterized using x-ray diffraction using $\text{Cu K}\alpha_1$ radiation ($\lambda = 1.5406\ \text{\AA}$). Fig. 3 shows the x-ray diffraction data of the InSb NWs. All the diffraction peaks (except the one with a * mark and peaks corresponding to Al_2O_3 template) were indexed according to the zinc blende crystal structure of bulk InSb from the JCPDS file. The peak with * mark at $2\theta \sim 33.2^\circ$ may be attributed to $\langle 321 \rangle$ peak of In_2O_3 or $\langle 101 \rangle$ peak of In or to both the impurity phases in host InSb. The lattice constant along different lattice planes was calculated and the average lattice constant was estimated to be $6.4450\ \text{\AA}$ with a 1.05% mismatch between the measured and standard reported value of InSb (see supplementary material Sec. A3⁵⁶). Both crystallite size (c) and the strain (e) contribution to the total contribution of line broadening were calculated using Scherrer formula³⁷

$$(B\cos\theta/\lambda) = (0.9/c) + (4e\sin\theta/\lambda),$$

$$B = (0.9\lambda/c \cos\theta) + (4e\tan\theta).$$

The first term on the right side of the latter equation is the line broadening contribution due to the crystallite size and the second one is due to the strain/distortions in the crystallite. λ is the $\text{Cu K}\alpha_1$ wavelength, θ is the Bragg diffraction angle corresponding to particular diffraction peak, c is the crystallite size, and e is the maximum limit to the strain in the lattice along the particular diffraction direction. B , the total contribution to the line broadening, can be experimentally measured from the full width at half maximum for any particular diffraction direction and c and e can be estimated from intercept and the slope of the Williamson-Hall straight line plot between $(B \cos\theta/\lambda)$ vs. $(\sin\theta/\lambda)$. Williamson-Hall plot for the electrodeposited nanowires was plotted after fitting all the diffraction peaks to a Pearson VII amplitude profile using peakfit software and is shown in Fig. 3 (inset). The linear plot with finite positive slope indicates the presence of

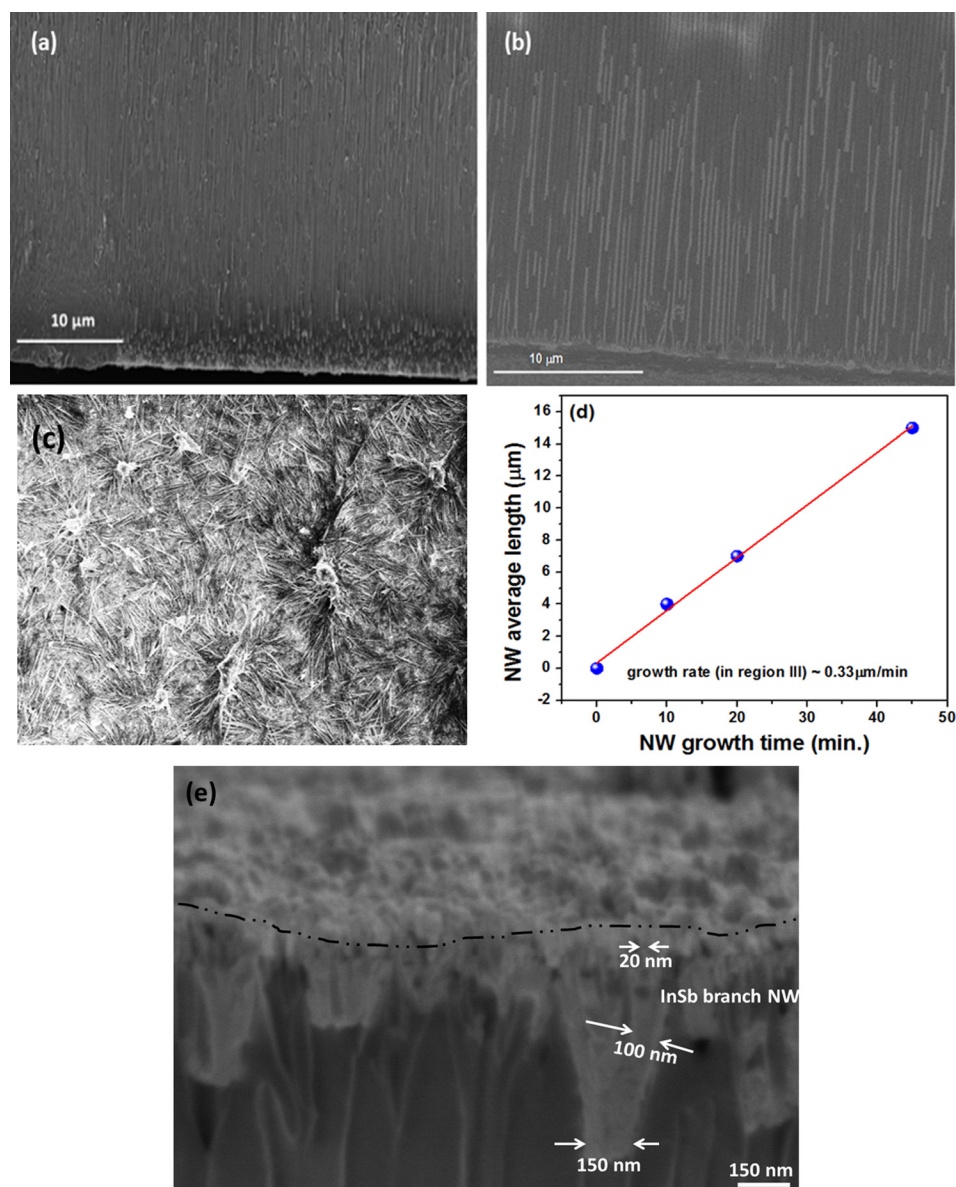


FIG. 2. Cross-sectional FESEM image of InSb nanowires embedded inside the nanochannels of a PAA template, following growth at a lower electrode potential of -1.0 V for (a) 20 min and (b) 45 min. (c) Top view FESEM image of InSb nanowire arrays after etching back the PAA matrix with 1 M KOH; (d) average NW length vs. NW growth time (min) plot in region III to estimate the growth rate of NW arrays in region III; (e) high resolution FESEM showing representative hierarchical BNW array.

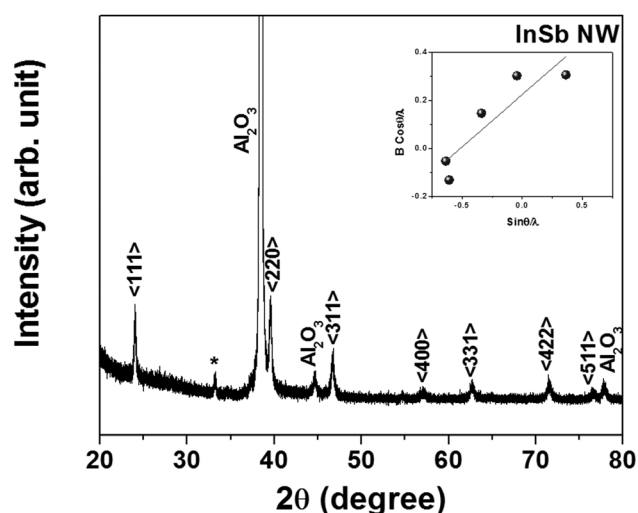


FIG. 3. Powder x-ray diffraction pattern of annealed InSb nanowire array (grown at -1.5 V) using Cu K α 1 radiation ($\lambda = 1.5406$ Å); inset shows the corresponding Williamson-Hall plot showing line broadening from lattice strain and crystallite size.

the both line broadening factors in our InSb nanowires. The crystallite size and the lattice strain were found to be 4.011 nm and 0.109, respectively.

In order to probe the detailed microstructures of the tailored branched NW structure, surface roughness, crystal orientations, lattice structure, etc., High Resolution Transmission Electron Microscopy (HRTEM), EDX analysis, and Raman spectroscopy of the electrodeposited InSb NWs were performed.

Figures 4(a)–4(d) show the HRTEM image along with the FFT analysis of representative InSb BNWs. Images were taken within both the branched and the trunk region of the wires. Figure 4(a) shows the HRTEM image of a RT as-grown NW taken at the thicker trunk region. For clarity, the full NW diameter is shown in the inset with the zoomed-in portion of the wire (indicated in solid box located at the edge of the NW) where HRTEM measurements were performed. The as-grown wires form an amorphous-rich outer edge, while the nanocrystalline regions are present towards the interior of the body of the wires. Selective area electron

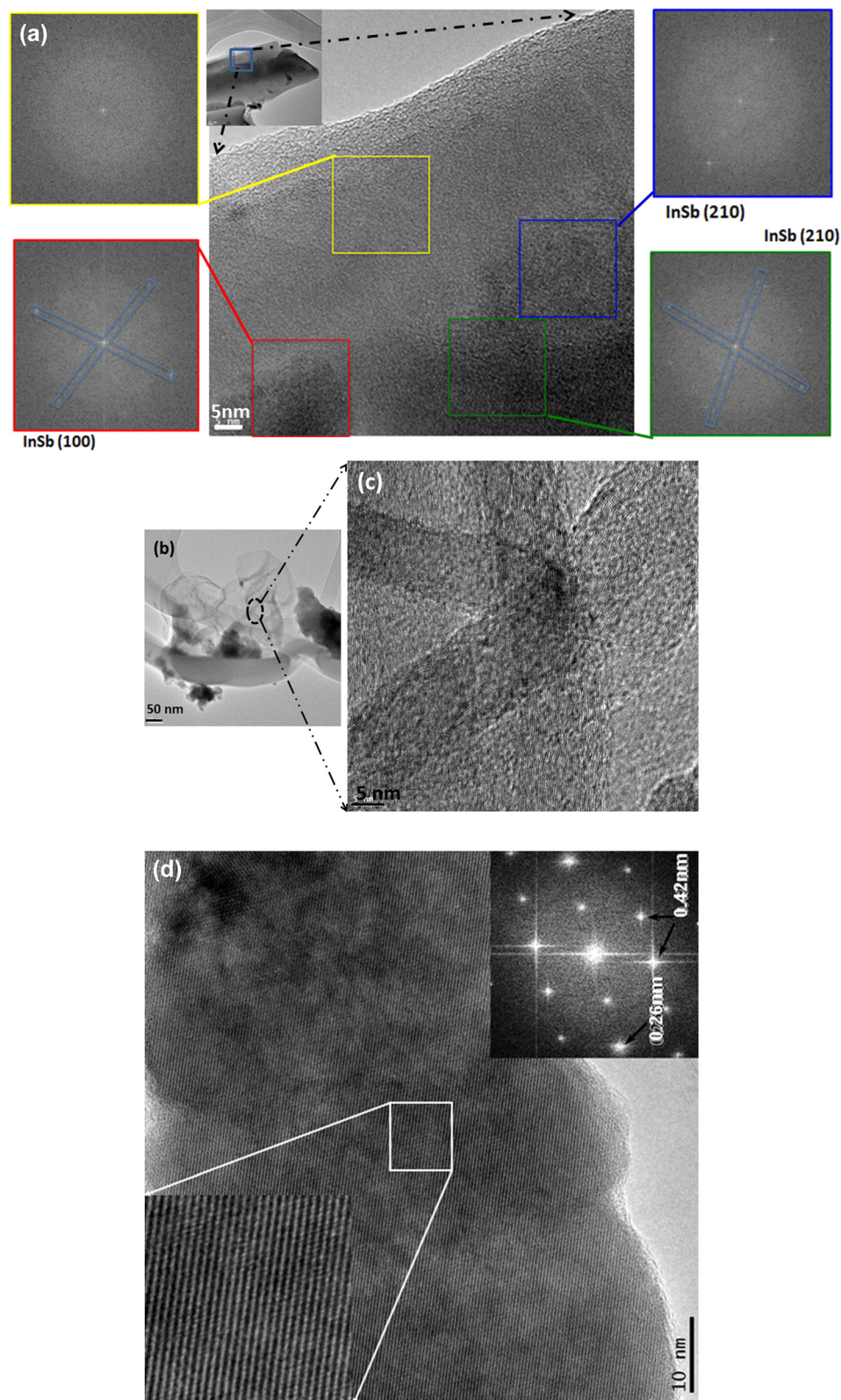


FIG. 4. (a) HRTEM image of trunk region of an as-grown InSb NW grown at RT and at -1.5 V; inset shows the complete NW structure and the solid box at its one edge shows the HRTEM imaging region of interest. Both amorphous and nanocrystalline regions (of InSb phase) with different crystallographic orientation were identified from the SAED patterns at various locations as shown; (b) low resolution TEM image of as-grown nanowires, following removal from PAA template. A number of NW segments ("trunks" and "branches") are visible in image; (c) zoom-in portion of Fig. 4(b) at a spot showing the smaller diameter segments ("branches"), indicating that these regions are crystalline even prior to annealing; (d) HRTEM image of a segment of a trunk region of InSb NW after thermal annealing. The lower part of Fig. 4(d) shows a magnified view of the parallel lattice planes of zinc blende InSb NW, indicating parallel lattice planes along $\langle 111 \rangle$ direction.

diffraction (SAED) patterns at various locations on the NW body are collected and are shown in the enclosed boxes. Complete outer edge of the NW exhibits a characteristic electron diffraction pattern as depicted in the yellow box. This featureless diffraction pattern indicates non-crystalline nature of the region. Other regions selected in the figure show diffraction patterns as indicated by the lattice indices of InSb. The disparity in these patterns with each other

suggests that these regions exhibit different crystallite orientations. It is clear that the RT growth of thick InSb NWs produces wires with nanocrystalline structures, with randomly oriented nanocrystals. Figure 4(b) shows a low resolution image of number of wires entangled within the TEM grid, containing segments of both trunks and branches. Figure 4(c) shows the HRTEM images of the branch regions of the as-grown BNWs. The branches are 10–15 nm in diameter and

are crystalline, as indicated by the parallel lattice planes. Several branched NWs flocking together can be seen in the image, all are sub-20 nm diameter. The nucleation of InSb at the pore-bottoms of tiny channels, subsequent growth and crystallization at RT may be due to confinements of crystal planes in the reduced dimensional channels. Recently, nucleation and crystal growth under nanoscale confinement have been investigated and reported. A crystallization of organic compounds in nanoporous matrices is reviewed by Jiang *et al.*³⁸ The authors correlate the competitive nucleation (kinetics of crystallization vs. the thermodynamics of nucleation) in the confined pores and argued for a preferred orientation of nanocrystals growth in anodic alumina templates. Although the report entirely involves templates with parallel pores and organic compounds, our study on branch nanowires, tailored diameter and underlying InSb nanowire crystallization should have a similar growth mechanism.

Figure 4(d) shows a HRTEM image of a segment of the trunk in a post-annealed wire. Remarkably, in this case, the structure has transformed to being single crystalline along the entire length of the NW, without any visible dislocations, twin defects, or stacking faults, etc. The magnified part (lower part of Fig. 4(d)) shows the growth along [111] direction of the NW. This assignment is confirmed from the interplanar spacing value of $d_{hkl} = a/(h^2 + k^2 + l^2)^{1/2}$ for [111] direction and using the lattice parameter found from x-ray diffraction. The FFT analysis of the NW reveals the SAED pattern of the InSb zinc blende crystal structure. However, one notices that the NW surface is not atomically smooth; rather the surface roughness varies between 5 and 7 nm along the NW length.

Fig. 5 shows the EDX analysis of InSb NW. Both the elemental analysis and the energy spectrum of the core-electrons

of the elements are shown. Uniform spatial distribution of indium and antimony over the NW body (characterized by red and cyan dots, respectively, in the elemental analysis) reveals the compositional uniformity of the constituent elements in the NW. The presence of oxygen is characterized by the white dots, which often come from the outer oxide shell present on the NW. The carbon atoms get deposited on the NW as a result of very high resolution spectroscopic imaging and are characterized by the green dots in the elemental analysis. The spectrum in Fig. 5 shows the various peaks corresponding to the constituent indium and antimony in the wire.

Fig. 6 shows the scanning TEM image of an InSb NW with ~ 10 nm diameter along with the SAED pattern (Figs. 6(a) and 6(b)). The nanowire is highly crystalline with a growth direction along [311]. This direction was obtained by comparing the SAED pattern with the theoretical diffraction pattern of InSb (ICSD code: 640411) shown in Fig. 6(c). Parallel lattice planes along (111) direction are well resolved and the measured interplanar spacing is 0.36 nm ($d_{hkl} = a/(h^2 + k^2 + l^2)^{1/2} = 6.4789/\sqrt{3} = 3.74 \text{ \AA} \sim 0.36 \text{ nm}$), which corresponds to InSb crystal. A comparison of measured interplanar spacing from FFT (Fig. 6(d)) with the theoretical one (Fig. 6(c)) shows a 9% lattice relaxation in the NW.

For InSb nanowire lattice properties (zinc-blende crystal structure), the NW array was studied by analyzing their phonon spectra using Raman spectroscopy. Figure 7(a) shows the Raman spectra of InSb NWs ensemble with different incident laser powers and in Figure 7(b) the corresponding spectra of a bulk InSb wafer (111) is presented for comparison. The peak around $175\text{--}177 \text{ cm}^{-1}$ in bulk InSb corresponds to the TO phonon and the one at around 187 cm^{-1} corresponds to the LO phonon mode.³⁹ Similar features were observed in our InSb nanowires in addition to few other

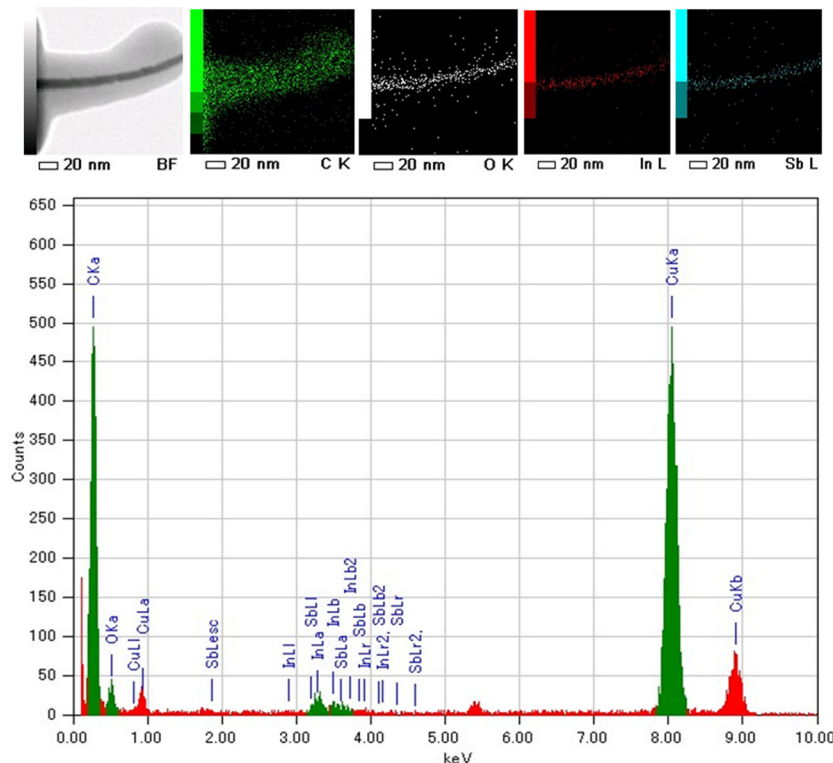


FIG. 5. EDX elemental mapping and EDX spectrum of single InSb NW (grown at -1.5 V) captured using a detector inside the STEM chamber. Contribution from carbon is coming after interaction of high energy electron beams with the nanowires.

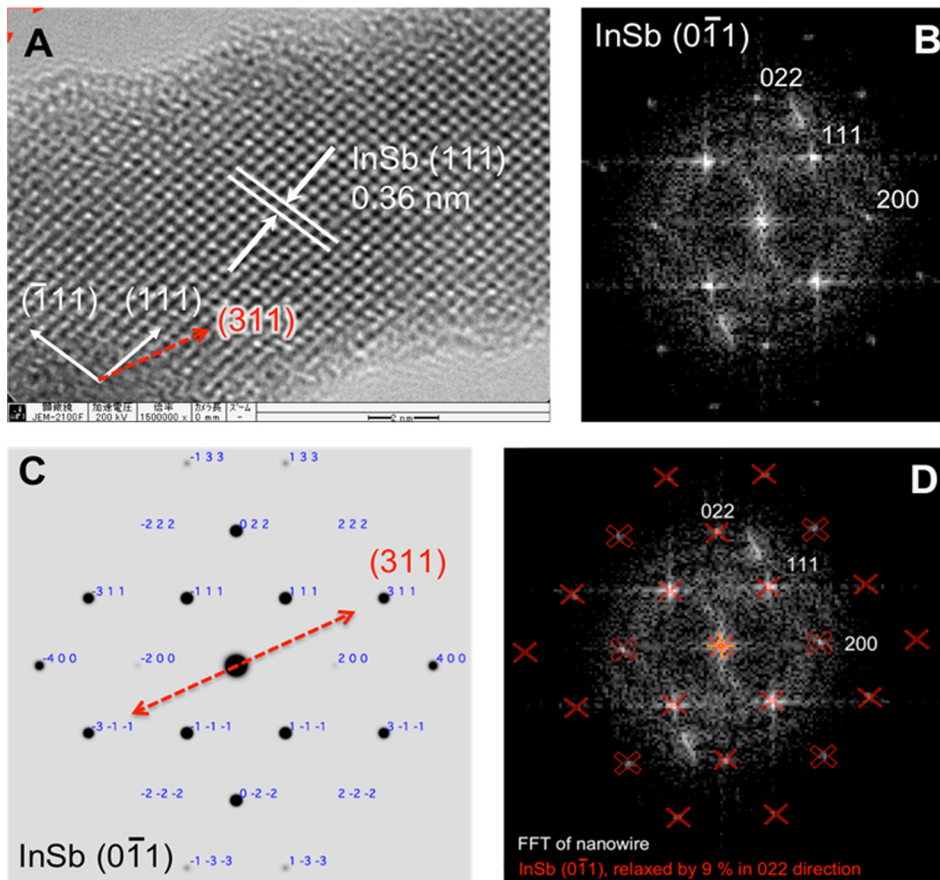


FIG. 6. (a) Scanning Transmission Electron Microscopic (STEM) image of a sub-10 nm ultra-thin InSb nanowire (grown at -1.5 V), showing InSb zinc-blende structure. The ultra-thin branch after annealing grows along $\langle 311 \rangle$ direction (shown by the red arrow); (b) SAED pattern showing the diffraction points of InSb NW; (c) the theoretical diffraction of zinc-blende InSb; (d) comparison of the experimentally measured InSb NW with the theoretical diffraction spots.

peaks. In order to identify the exact peak positions, we have fitted the peaks of the spectrum—taken at 16 mW laser power—using a Lorentzian line shape analysis, see Fig. 7(c). A similar procedure was followed for the spectra taken at other laser powers as well. Solid spheres represent the experimental data and the lines represent the results of the Lorentzian line shape analysis for the complete spectrum, the individual peak positions, and FWHM. The peaks at 175.2 cm^{-1} and 185.33 cm^{-1} represent both the TO and LO positions, respectively, for InSb NWs. However, we must be emphasizing a number of important differences between bulk and NW InSb: First, the peaks in the bulk InSb are symmetric, whereas the peaks in the nanowires were found to be asymmetric with appearance of low frequency tail. Second, there are peak shifts in each of these peaks compared to the bulk values. Third, after calculating the FWHM of the peaks, it was realized that the line widths of the peaks in the nanowires are broadened. And lastly, the peaks at 134.15 cm^{-1} and 104.35 cm^{-1} are not visible in the bulk InSb, but are prominent in our InSb NWs. For an ideal infinite bulk crystal, the Raman scattering occurs because of the participation of phonons centered on the Brillouin zone center (this gives rise to fundamental $q \sim 0$ Raman selection rule). However, when the crystal size reduces to nanoscale as in nanowires, due to Heisenberg uncertainty principle, the $q=0$ Raman selection rule gets relaxed and phonons away from Brillouin zone participate in the scattering. The phonon uncertainty which varies $\Delta q \sim 1/d$ (d is the nanowires diameter) and gives rise to asymmetric broadening and downshifting of the Raman peaks.

Similar situations also arise for crystals with large crystal imperfections (like roughness), impurities, and defects. The appearance of additional peaks at $\sim 150\text{ cm}^{-1}$ and $\sim 110\text{ cm}^{-1}$ was reported earlier in InSb nanorods by Wada *et al.*; these peaks have been assigned to TO-TA and 2TA phonon modes, respectively.⁴⁰ Also, the room temperature Sb A_{1g} and E_g peak positions are reported at $\sim 150\text{ cm}^{-1}$ and $\sim 110\text{ cm}^{-1}$, respectively.^{41,42} Berengue *et al.* recently reported the Raman spectra of cubic In_2O_3 NWs, which shows phonon modes at 109 cm^{-1} and 135 cm^{-1} and Deng *et al.* showed the phonon modes of (rectangular cross-section) Sb_2O_3 NWs, which appear at 143.69 cm^{-1} .^{43,44} Since our InSb NW is fairly phase pure, we do not assign the peaks to any of the impurity peaks pertaining to Sb, In_2O_3 , and Sb_2O_3 . On other hand, Kiefer *et al.* assigned all the phonon modes in bulk InSb at RT, with the peaks at 134 cm^{-1} and $\sim 120\text{ cm}^{-1}$ assigned to TO-TA and 2TA phonon modes, respectively.⁴⁵ Therefore, we assign the peaks at 134.15 cm^{-1} to TO-TA mode and at 104.35 cm^{-1} to 2TA mode. Although $\sim 15\text{ cm}^{-1}$ Raman shift in the peak position is large and is not expected to occur only due to phonon confinement (from $\sim 150\text{ nm}$ wires to \sim sub 20 nm wires), the residual stress and strain in our hierarchical branched structures may account for this shift. Because of the merging of many branches on NW trunk and also because of the tapering of the trunk itself there might be a large residual stress present in the structure. A large downshift of $\sim 40\text{ cm}^{-1}$ has been previously noticed in the LO mode of GaAs NWs by Shi *et al.* and has been assigned to defects and residual stresses in addition to the phonon confinement.⁴⁶ The downshifting

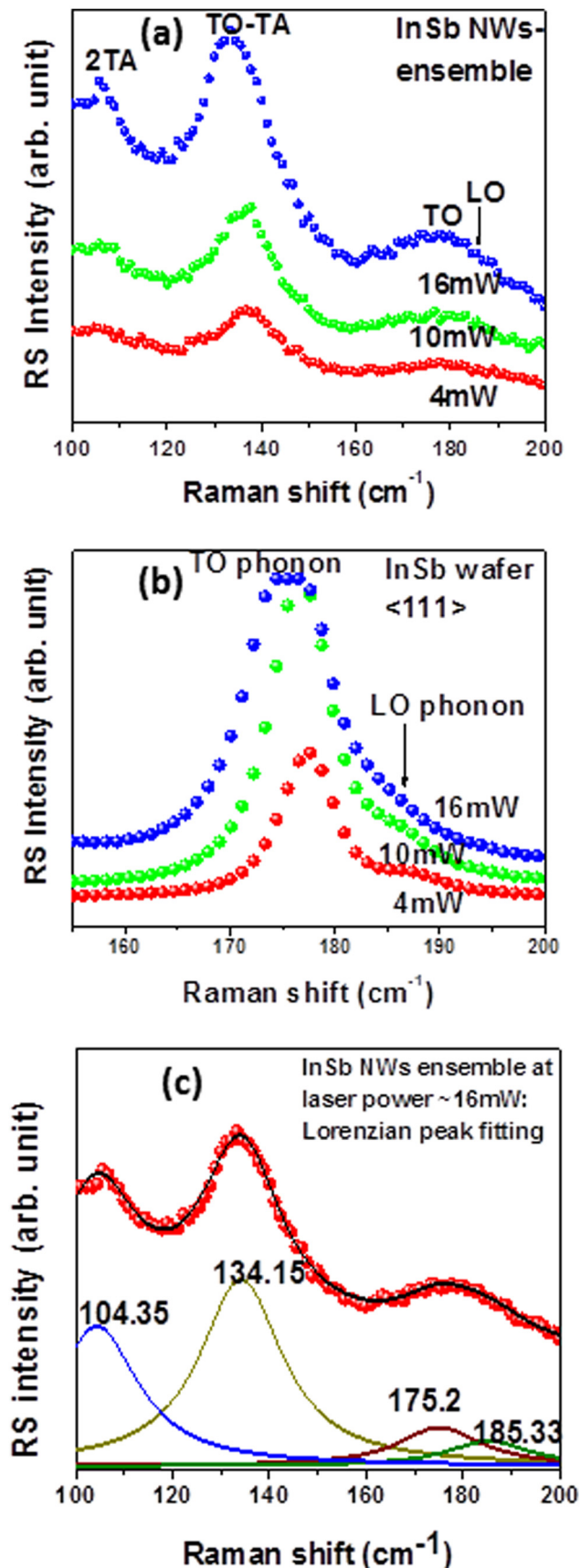


FIG. 7. (a) Raman spectrum in backscattered geometry at different power densities for annealed InSb BNW array; (b) the corresponding Raman spectrum of bulk InSb wafer <111> was taken at same experimental setting using similar parameters; (c) de-convolution of InSb Raman spectrum into various phonon modes using Lorentzian line shape analysis (spectrum with 16 mW laser power).

(and asymmetric broadening) of the LO and TO peak positions and hence the phonon energy in our InSb NWs with different laser power can be related to the combined effect of phonon-confinement (Richter-Campbell-Fauchet model) and lattice heating of the wires (photoexcitation of carriers and dissipation of excess heat to the lattice). Similar results were reported for Si nanowires by Piscanec *et al.*⁴⁷ Our very thin/small diameters of BNWs can cause significant phonon confinement leading to few cm⁻¹ downshifting in Raman peaks. Like nanostructures, the lack of long range order induced by other non-idealities in crystal structures like impurities, lattice defects, and/or surface roughness, further downshifts the phonon peaks compared to the bulk values. Since the HRTEM and XRD results of our InSb NWs reveal no existence of lattice defects and impurities, the further downshifting in the phonon peaks is believed to be due to the residual stress, strain, and surface roughness in our NWs in addition to the phonon confinements.

D. Branched NWs as an anti-reflective layer

Recently, NW arrays with different shape, structures, and of different materials have demonstrated unprecedented potential for applications such as photovoltaics, water splitting to produce hydrogen and oxygen, and photon management studies apart from cost effectiveness and material consumption issue (e.g., Si NW array would typically need 10%–15% materials for same efficiency solar cell as a 300 μm thin film silicon solar cell).^{48–53} One of the most striking properties of NW arrays is the low reflectance property which immediately attracts them for using as antireflection coatings. Recently, InP NW arrays were used to build solar cells with 13% efficiency.⁵⁴ InSb NW arrays, on other hand because of its very low room temperature bandgap energy (even in a 1D quantization limit of ~ 23 nm diameter wires, its bandgap increases only by ~ 100 meV) could be useful for probing mid-IR regime and thus useful for developing IR imagers and detectors. We measured the broadband reflectance of the BNW array and compared with the corresponding bulk values (<111> InSb wafer). Assuming the average refractive index of InSb 4.313, the reflectance of a bulk InSb is given as follows:

$$R_{\text{InSb(Bulk)}} = \left(\frac{n_{\text{InSb}} - n_{\text{Air}}}{n_{\text{InSb}} + n_{\text{Air}}} \right)^2 = \left(\frac{4.313 - 1}{4.313 + 1} \right)^2 = 0.3888 = 38.88\%.$$

Figure 8(a) shows the experimental reflectance of a bulk InSb wafer and matches well with the predicted reflectance of $\sim 39\%$. The artifact, shown by large variation, in the data is due to the change of the source between tungsten-halogen and deuterium at around ~ 700 nm as well as around ~ 2300 nm. Figure 8(b) shows the corresponding reflectance spectrum of BNW array and the inset shows the FESEM image of BNW array in which PAA is back-etched a micron depth to reveal the branch structure for the reflectance measurements. The reduction of average reflectance from $\sim 40\%$ to 4%–5% in BNW array indicates the potential use of this structure in antireflection coating using

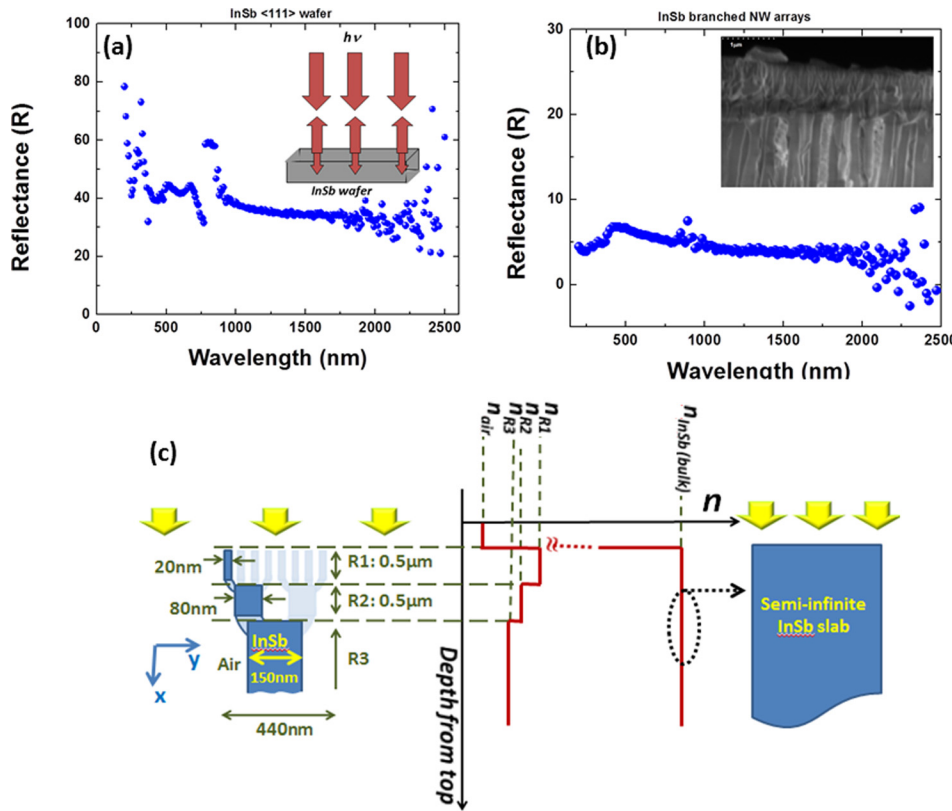


FIG. 8. UV-VIS-IR reflectance spectrum of (a) bulk InSb (wafer) and (b) InSb BNW array. Inset in Fig. 8(b) shows a cross sectional FESEM image of an array with PAA etched back from the top surface. Fig. 8(c) shows the change in refractive index of the medium as seen by light as it approaches and passes through the branched nanowires. For comparison of impedance mismatch, a bulk InSb picture is included in the figure.

InSb. The broadband nature of the reflectance also indicates its potential use in UV-VIS and in IR regime. In order to understand the reflectance spectrum, we show in Figure 8(c) the qualitative refractive index profile of BNW array based on effective medium theory approximation. A side-by-side comparison with a bulk InSb slab is also shown in the figure. Excellent anti-reflecting properties can be realized in the BNW array by the tailored refractive index formed due to the structure, leading to a better impedance matching compared to the bulk InSb. We also simulated the bulk structure and BNW array using electromagnetic simulator COMSOL RF-module. Bulk InSb refractive index values at different wavelengths were calculated and used for the BNW structure (see Fig. A3 in Sec. A5 of supplementary material⁵⁶). The result is shown in Fig. 9. Simulation results in Figs. 9(a) and 9(b) match well the experimental results for BNW array and bulk InSb. The presence of peaks and oscillations in reflectance in bulk InSb at lower wavelength values (below 700 nm) matches with modeling results shown in Fig. 9(b). For clarity, the BNW reflectance was again shown along with the simulation result in Fig. 9(a) and the schematic diagram of the BNW array is shown in Fig. 9(a) inset. The periodic peaks in the simulation result come from the resonances of NW pitch in the simulation sample; however, in the actual sample, especially in the top branches of InSb NWs, since the pitch is randomized so we get a smooth reflectance spectrum in the experiment. However, the average value of reflectance obtained from the simulation matches quite well with the experiment. The manipulation of high-index materials (e.g., InSb) in

unique nanostructured form not only reduces the reflectance from the surface but also has a number of interesting photonic properties such as tunable light absorption, enhanced light trapping and scattering events. These new nanophotonic physics in subwavelength scale can readily be exploited in efficient photon managements in number of applications such as photovoltaics, photocatalysis, and IR detectors.^{36,55}

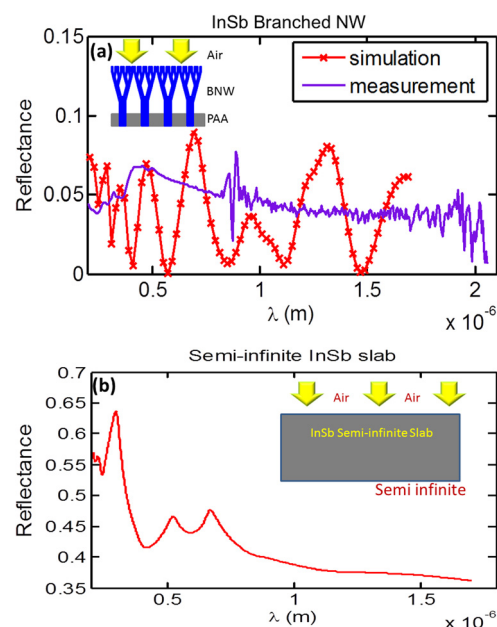


FIG. 9. (a) Simulated and measured spectra for the BNW array schematically shown in the inset using COMSOL-RF module; (b) simulated reflectance spectrum of a semi-infinite InSb slab.

IV. CONCLUSION

Single crystalline straight and branched InSb nanowires of zinc-blende crystal structures with diameter of sub-10 nm to ~ 150 nm were grown at room temperatures using a DC electrodeposition. As-grown thin branched wires are crystalline, whereas the thicker wires are nanocrystalline; however, post-deposition annealing in argon at 420°C produced crystalline InSb NWs along $\langle 111 \rangle$ direction for thicker wires and along $\langle 311 \rangle$ direction for ultra-thin nanowires. Structural characteristics were investigated using x-ray diffraction, TEM, Scanning Transmission Electron Microscopic (STEM), EDX, and Raman spectroscopy, all of which confirmed the crystal structure of the InSb nanowires. These structurally tailored BNWs and BNW arrays are characterized by unique physical properties. With a simple optical reflectance measurements and comparison with the similar results from a bulk InSb wafer, it is evident that such an array acts as an antireflection coating and could be useful for nanostructured energy harvesting and photon management studies. In addition, this nano-architected template-assisted hierarchically branched InSb NWs of varying diameters of ~ 10 – 20 nm, 80 – 100 nm, and 150 – 200 nm, could be useful for growing BNWs and BNW arrays of any arbitrary materials compatible with electrodeposition.

ACKNOWLEDGMENTS

This work was supported by Center for Re-Defining Photovoltaic Efficiency through Molecule Scale Control, an Energy Frontier Research Center (EFRC) funded by the U.S. Department of Energy, Office of Science, Office of Basic Energy Sciences, under Award 2(ACCT5-64852) and by National Science Foundation under Grant Nos. ECCS-1202281 and ECCS-1118934.

- ¹Y. Zhao, D. Canebat, C. Delker, Y. Zi, D. Janes, J. Appenzeller, and C. Yang, *Nano Lett.* **12**, 5331–5336 (2012).
- ²Y. Huang, X. Duan, and C. M. Lieber, *Small* **1**, 142–147 (2005).
- ³Z. Fan, H. Razavi, J.-W. Do, A. Moriwaki, O. Ergen, Y.-L. Chueh, P. W. Leu, J. C. Ho, T. Takahashi, L. A. Reichertz, S. Neale, K. Yu, M. Wu, J. W. Ager, and A. Javey, *Nature Mater.* **8**, 648–653 (2009).
- ⁴J. H. Seol, A. L. Moore, S. K. Saha, F. Zhou, L. Shi, Q. L. Ye, R. Scheffler, N. Mingo, and T. Yamada, *J. Appl. Phys.* **101**, 023706 (2007).
- ⁵L. Xu, Z. Jiang, Q. Qing, L. Mai, Q. Zhang, and C. M. Lieber, *Nano Lett.* **13**, 746–751 (2013).
- ⁶R. S. Wagner and W. C. Ellis, *Appl. Phys. Lett.* **4**, 89–90 (1964).
- ⁷M. Tian, J. Wang, J. Kurtz, T. E. Mallouk, and M. H. W. Chan, *Nano Lett.* **3**, 919–923 (2003).
- ⁸H. Yu and W. E. Buhro, *Adv. Mater.* **15**, 416–419 (2003).
- ⁹K. G. Biswas, H. E. Matbouly, V. Rawat, J. L. Schroeder, and T. D. Sands, *Appl. Phys. Lett.* **95**, 073108 (2009).
- ¹⁰G. Meng, Y. J. Jung, A. Cao, R. Vajtai, and P. M. Ajayan, *Proc. Natl. Acad. Sci. U.S.A.* **102**, 7074–7078 (2005).
- ¹¹M. Paladugu, J. Zou, Y. N. Guo, X. Zhang, Y. Kim, H. J. Joyce, Q. Gao, H. H. Tan, and C. Jagadish, *Appl. Phys. Lett.* **93**, 101911 (2008).
- ¹²J. E. Allen, E. R. Hemesath, D. E. Perea, J. L. Lensch-Falk, Z. Y. Li, F. Yin, M. H. Gass, P. Wang, A. L. Bleloch, R. E. Palmer, and L. J. Lauhon, *Nat. Nanotechnol.* **3**, 168–173 (2008).
- ¹³J. B. Hannon, S. Kodambaka, F. M. Ross, and R. M. Tromp, *Nature* **440**, 69–71 (2006).
- ¹⁴S. A. Dayeh, N. H. Mack, J. Y. Huang, and S. T. Picraux, *Appl. Phys. Lett.* **99**, 023102 (2011).
- ¹⁵E. Dailey, P. Madras, and J. Drucker, *J. Appl. Phys.* **108**, 064320 (2010).
- ¹⁶U. Philipose, G. Sapkota, P. Gali, and P. Nukala, *MRS Proc.* **1302**, mrsf10-1302-w09-31 (2011).
- ¹⁷X. Zhang, Y. Hao, G. Meng, and L. Zhang, *J. Electrochem. Soc.* **152**, C664–C668 (2005).
- ¹⁸J. Ortega and J. Herrero, *J. Electrochem. Soc.* **136**, 3388–3391 (1989).
- ¹⁹M. I. Khan, M. Penchev, X. Jing, X. Wang, K. N. Bozhilov, M. Ozkan, and C. S. Ozkan, *J. Nanoelectron. Optoelectron.* **3**, 199–202 (2008).
- ²⁰S. R. Das, C. J. Delker, D. Zakharov, Y. P. Chen, T. D. Sands, and D. B. Janes, *Appl. Phys. Lett.* **98**, 243504 (2011).
- ²¹Y.-L. Chueh, Z. Fan, K. Takei, H. Ko, R. Kapadia, A. A. Rathore, N. Miller, K. Yu, M. Wu, E. E. Haller, and A. Javey, *Nano Lett.* **10**, 520–523 (2010).
- ²²J. Zhu, Z. Yu, G. F. Burkhard, C.-M. Hsu, S. T. Connor, Y. Xu, Q. Wang, M. McGehee, S. Fan, and Y. Cui, *Nano Lett.* **9**, 279–282 (2009).
- ²³Z. Fan, R. Kapadia, P. W. Leu, X. Zhang, Y.-L. Chueh, K. Takei, K. Yu, A. Jamshidi, A. A. Rathore, D. J. Ruebusch, M. Wu, and A. Javey, *Nano Lett.* **10**, 3823–3827 (2010).
- ²⁴J. Zhu, H. Peng, A. F. Marshall, D. M. Barnett, W. D. Nix, and Y. Cui, *Nat. Nanotechnol.* **3**, 477–481 (2008).
- ²⁵Y. Jung, D.-K. Ko, and R. Agarwal, *Nano Lett.* **7**, 264–268 (2007).
- ²⁶K. Seo, M. Wober, P. Steinvurzel, E. Schonbrun, Y. Dan, T. Ellenbogen, and K. B. Crozier, *Nano Lett.* **11**, 1851–1856 (2011).
- ²⁷P. M. Wu, N. Anttu, H. Q. Xu, L. Samuelson, and M.-E. Pistol, *Nano Lett.* **12**, 1990–1995 (2012).
- ²⁸H. Chen, X. Sun, K. W. C. Lai, M. Meyyappan, and N. Xi, in *IEEE Nanotechnology Materials and Devices Conference (NMDC), East Lansing, MI, USA, 2–5 June 2009*, pp. 212–216.
- ²⁹N. Mingo, *Appl. Phys. Lett.* **84**, 2652–2654 (2004).
- ³⁰I. V. Weperen, S. R. Plissard, E. P. A. M. Bakkers, S. M. Frolov, and L. P. Kouwenhoven, *Nano Lett.* **13**, 387–391 (2013).
- ³¹J. Alicea, *Phys. Rev. B* **81**, 125318 (2010).
- ³²V. Mourik, K. Zuo, S. M. Frolov, S. R. Plissard, E. P. A. M. Bakkers, and L. P. Kouwenhoven, *Science* **336**, 1003–1007 (2012).
- ³³P. Caroff, M. E. Messing, B. M. Borg, K. A. Dick, K. Deppert, and L. E. Wernersson, *Nanotechnology* **20**, 495606 (2009).
- ³⁴A. Pitanti, D. Coquillat, D. Ercolani, L. Sorba, F. Teppe, W. Knap, G. De Simoni, F. Beltram, A. Tredicucci, and M. S. Vitiello, *Appl. Phys. Lett.* **101**, 141103 (2012).
- ³⁵A. Ghahremaninezhad and A. Dolati, *ECS Trans.* **28**, 13–25 (2010).
- ³⁶A. Mohammad, S. R. Das, M. R. Khan, M. A. Alam, and D. B. Janes, *Nano Lett.* **12**, 6112–6118 (2012).
- ³⁷B. D. Cullity and S. R. Stock, *Elements of X-Ray Diffraction*, 3rd ed. (Prentice-Hall, New York, 2001), 664 pp.
- ³⁸Q. Jiang and M. D. Ward, *Chem. Soc. Rev.* **43**, 2066–2079 (2014).
- ³⁹A. Pinczuk and E. Burstein, *Phys. Rev. Lett.* **21**, 1073–1075 (1968).
- ⁴⁰N. Wada, H. Takayama, and S. Morohashi, in APS March meeting 55, Portland, Oregon, March 15–19 2010, Abstract No. L9.013.
- ⁴¹J. S. Lannin, J. M. Calleja, and M. Cardona, *Phys. Rev. B* **12**, 585–593 (1975).
- ⁴²U. Rettweiler, W. Richter, U. Resch, J. Geurts, R. Sporken, P. Xhonneux, and R. Caudano, *J. Phys: Condens. Matter* **1**, SB93–SB97 (1989).
- ⁴³O. M. Berengue, A. D. Rodrigues, C. J. Dalmaschio, A. J. C. Lanfredi, E. R. Leite, and A. J. Chiquito, *J. Phys. D: Appl. Phys.* **43**, 045401 (2010).
- ⁴⁴Z. Deng, F. Tang, D. Chen, X. Meng, L. Cao, and B. Zou, *J. Phys. Chem. B* **110**, 18225–18230 (2006).
- ⁴⁵W. Kiefer, W. Richter, and M. Cardona, *Phys. Rev. B* **12**, 2346–2354 (1975).
- ⁴⁶W. S. Shi, Y. F. Zheng, N. Wang, C. S. Lee, and S. T. Lee, *Appl. Phys. Lett.* **78**, 3304–3306 (2001).
- ⁴⁷S. Piscanec, M. Cantoro, A. C. Ferrari, J. A. Zapien, Y. Lifshitz, S. T. Lee, S. Hofmann, and J. Robertson, *Phys. Rev. B* **68**, 241312 (2003).
- ⁴⁸E. Garnett and P. Yang, *Nano Lett.* **10**, 1082–1087 (2010).
- ⁴⁹K. X. Wang, Z. Yu, V. Liu, Y. Cui, and S. Fan, *Nano Lett.* **12**, 1616–1619 (2012).
- ⁵⁰K. Sun, X. Pang, S. Shen, X. Qian, J. S. Cheung, and D. Wang, *Nano Lett.* **13**, 2064–2072 (2013).
- ⁵¹H. M. Chen, C. K. Chen, Y.-C. Chang, C.-W. Tsai, R.-S. Liu, S.-F. Hu, W.-S. Chang, and K.-H. Chen, *Angew. Chem.* **122**, 6102–6105 (2010).
- ⁵²S.-K. Kim, R. W. Day, J. F. Cahoon, T. J. Kempa, K.-D. Song, H.-G. Park, and C. M. Lieber, *Nano Lett.* **12**, 4971–4976 (2012).
- ⁵³D. M. Callahan, J. N. Munday, and H. A. Atwater, *Nano Lett.* **12**, 214–218 (2012).

⁵⁴J. Wallentin, N. Anttu, D. Asoli, M. Huffman, I. Åberg, M. H. Magnusson, G. Siefer, P. Fuss-Kailuweit, F. Dimroth, B. Witzigmann, H. Q. Xu, L. Samuelson, K. Deppert, and M. T. Borgström, *Science* **339**, 1057–1060 (2013).

⁵⁵M. L. Brongersma, Y. Cui, and S. Fan, *Nature Mater.* **13**, 451–460 (2014).

⁵⁶See supplementary material at <http://dx.doi.org/10.1063/1.4893704> for cyclic voltammetry for finding the growth parameters (redox potentials) for InSb NWs, deposition of InSb branched nanowires, x-ray diffraction analysis, NW growth rate in region II of current vs. voltage characteristics, and the refractive index simulation for InSb.